Chinese Chemical Letters 33 (2022) 2270–2280

Contents lists available at ScienceDirect

Chinese Chemical Letters

journal homepage: www.elsevier.com/locate/cclet

Recent advances in carbon-based materials for electrochemical CO_2 reduction reaction

Zengqiang Gao[1], Junjun Li[1], Zhicheng Zhang*, Wenping Hu

Tianjin Key Laboratory of Molecular Optoelectronic Sciences, Department of Chemistry, School of Science & Collaborative Innovation Center of Chemical Science and Engineering, Tianjin University, Tianjin 300072, China

ARTICLE INFO

Article history:
Received 10 August 2021
Revised 4 September 2021
Accepted 9 September 2021
Available online 14 September 2021

Keywords:
CO_2 reduction
Electrocatalysis
Carbon materials
Chemicals and fuels
Single-atom catalysts

ABSTRACT

The increase of atmospheric CO_2 concentration has caused many environmental issues. Electrochemical CO_2 reduction reaction (CO_2RR) has been considered as a promising strategy to mitigate these challenges. The electrocatalysts with a low overpotential, high Faradaic efficiency, and excellent selectivity are of great significance for the CO_2RR. Carbon-based materials including metal-free carbon catalysts and metal-based carbon catalysts have shown great potential in the CO_2RR, owing to the tailorable porous structures, abundant natural resources, resistance to acids and bases, high-temperature stability, and environmental friendliness. In this review, various carbon materials including graphene, carbon nanotubes, quantum dots, porous carbon, and MOF-derived catalysts, *etc*., for the CO_2RR have been summarized. Particularly, recent progress in terms of the mechanism and pathway of CO_2 conversion has been comprehensively reviewed. Finally, the opportunities and challenges of carbon-based electrocatalysts for the CO_2RR are proposed.

1. Introduction

The fossil fuels supply about 75% of global energy demands, and the CO_2 emissions associated with excessive fossil fuel consumption resulted in global extremes, ocean acidification, and sea-level rise. Currently, the atmospheric CO_2 concentration has increased to 418.94 ppm in 2021 [1]. Converting CO_2 into sustainable fuels and chemical feedstocks, *via* biochemical, photocatalytic, and electrocatalytic reactions, *etc*., provides a promising approach to close the carbon cycle and alleviate energy and environmental problems. To date, electrocatalytic CO_2 reduction reaction (CO_2RR) has been considered as an important route to address the above-mentioned issues, because of its moderate conditions, controllable process, minimized chemical consumption, and easy-to-scale-up applications [2–5]. However, CO_2 has a stable molecular structure (high C=O dissociation energy of 803 kJ/mol), leading to a high kinetic barrier [6–8]. During the electrochemical reduction of CO_2, the multi-proton-coupled electron transfer processes usually generate a significant number of intermediates, resulting in low product selectivity. Therefore, the rational design and controlled synthesis of advanced electrocatalysts with high activity, selectivity, and stability are highly desired.

Until now, various electrocatalysts including noble metals, metal alloys, and transition metal oxides have been developed, exhibiting outstanding electrocatalytic performance for the CO_2RR. However, it remains a great challenge to fabricate the electrocatalyst with low cost, highly exposed active sites, and industrial-grade current densities. Up to now, carbon-based materials have been regarded as one of the most promising catalysts for the CO_2RR owing to the inherent advantages, such as abundant natural resources, resistance to acids and bases, high-temperature stability, and environmental friendliness. The tunable electronic structures and excellent electrical conductivity of carbon-based materials are viable to reduce the energy barrier for C–C coupling [9]. Despite the poor catalytic activity of carbon materials, their performance can be greatly improved *via* doping heteroatoms or constructing metal/carbon composites. More importantly, constructing carbon-based single-atom catalysts or tandem catalysts becomes a potential strategy to achieve a good catalytic activity, selectivity, as well as stability [10,11]. In this review, we have comprehensively summarized the recent development of metal-free and metal-based carbon materials for the CO_2RR, involving synthetic strategies, catalytic active sites, and reaction mechanisms.

* Corresponding author.
E-mail address: zczhang19@tju.edu.cn (Z. Zhang).
[1] These authors contributed equally to this work.

https://doi.org/10.1016/j.cclet.2021.09.037
1001-8417/

Table 1
The electrochemical thermodynamic reactions for CO_2 reduction and their corresponding standard redox potentials.

	Acid		Base	
Products	equation	*E* (V)	equation	*E* (V)
H_2	$2H^+ + 2e^- \rightarrow H_2$	0.000	$2H_2O + 2e^- \rightarrow H_2 + 2OH^-$	−0.828
CO	$CO_2 + 2H^+ + 2e^- \rightarrow CO + H_2O$	−0.104	$CO_2 + H_2O + 2e^- \rightarrow CO + 2OH^-$	−0.932
CH_4	$CO_2 + 8H^+ + 8e^- \rightarrow CH_4 + 2H_2O$	0.169	$CO_2 + 6H_2O + 8e^- \rightarrow CH_4 + 8OH^-$	−0.659
CH_3OH	$CO_2 + 6H^+ + 6e^- \rightarrow CH_3OH + H_2O$	0.016	$CO_2 + 5H_2O + 6e^- \rightarrow CH_3OH + 6OH^-$	−0.812
HCOOH	$CO_2 + 2H^+ + 2e^- \rightarrow HCOOH$	−0.171	$CO_2 + H_2O + 2e^- \rightarrow HCOO^- + OH^-$	−0.639
C_2H_4	$2CO_2 + 12H^+ + 12e^- \rightarrow C_2H_4 + 4H_2O$	0.085	$2CO_2 + 8H_2O + 12e^- \rightarrow C_2H_4 + 12OH^-$	−0.743
C_2H_6	$2CO_2 + 14H^+ + 14e^- \rightarrow C_2H_6 + 4H_2O$	0.144	$2CO_2 + 10H_2O + 14e^- \rightarrow C_2H_6 + 14OH^-$	−0.685
CH_3CH_2OH	$2CO_2 + 12H^+ + 12e^- \rightarrow CH_3CH_2OH + 3H_2O$	0.084	$2CO_2 + 9H_2O + 12e^- \rightarrow CH_3CH_2OH + 12OH^-$	−0.744
CH_3COOH	$2CO_2 + 8H^+ + 8e^- \rightarrow CH_3COOH + 2H_2O$	0.098	$2CO_2 + 5H_2O + 8e^- \rightarrow CH_3COO^- + 7OH^-$	−0.653
C_3H_7OH	$3CO_2 + 18H^+ + 18e^- \rightarrow CH_3CH_2CH_2OH + 5H_2O$	0.095	$3CO_2 + 13H_2O + 18e^- \rightarrow CH_3CH_2CH_2OH + 18OH^-$	−0.733

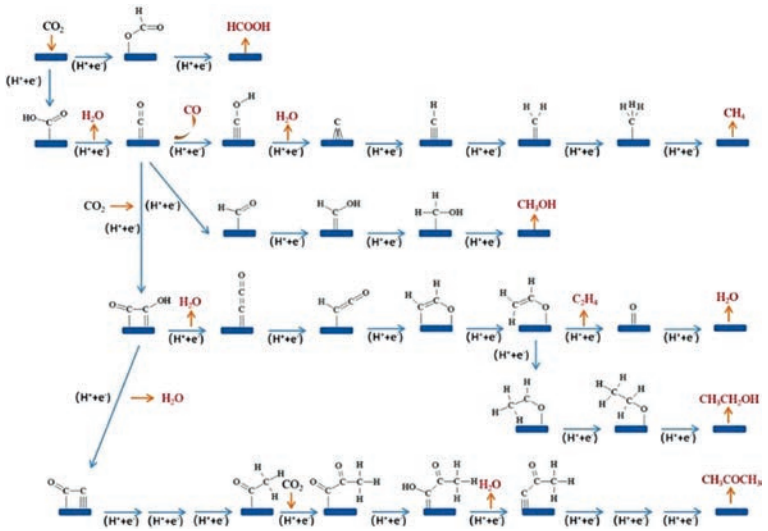

Fig. 1. The reaction pathways for the CO_2RR on the catalysts. Reproduced with permission [22]. Copyright 2021, Wiley-VCH.

2. The catalytic mechanisms for CO_2 reduction

The complex processes of electrochemical CO_2 reduction yield various reduction products. According to the number of carbon atoms, the reduction products can be classified as C_1 products (*e.g.*, CO and HCOOH), C_2 products (*e.g.*, C_2H_4, C_2H_6 and C_2H_5OH) and C_3 products (*e.g.*, C_3H_6 and C_3H_7OH). The value-added multi-carbon (C_{2+}) products are more favored over the C_1 products. The standard potentials for the conversion of CO_2 into different products are similar (Table 1) and the standard potential for H_2 within this range would decrease the selectivity for high-value products [12–14]. The principle of the CO_2RR contributes to investigate a favorable kinetic pathway to bypass the hurdles of the high overpotential and hinder the process of the HER. The reaction pathways of the CO_2RR are shown in Fig. 1. First, CO_2 is adsorbed on the surface of the catalysts, forming unstable $*CO_2^{\delta-}$ radicals which are readily protonated to generate bidentate intermediate (*OCHO) or adsorption intermediate (*COOH) [15,16]. For example, Song *et al.* found that the formation of *COOH and *CO are more beneficial on pyridinic N and pyrrolic N than that on graphite N and pure carbon. The energy for the *CO-to-*CHO conversion on pyridinic N sites is 0.82 eV, whereas it is a slight exothermicity of -0.24 eV on pyrrolic N sites, revealing that the formation of *CHO is thermodynamically advantageous on pyrrolic N [17]. Furthermore, the metal center with various d-electron structures on metal-based carbon materials exhibited unusual adsorption energies of CO_2-related intermediates *via* the fine-tuning of crystal facets, and chemical states, which can adsorb CO_2 or the related intermediates [18]. Then, the H^+ is adsorbed on $*CO_2^{\delta-}$ *via* a proton-coupled electron transfer process or hydrogenation towards different products. Significantly, *CO intermediates are crucial intermediates to produce multi-carbon products [19]. Since protons can be accepted by C and O, the reaction in this step is divided into two parts by the position of accepted protons: (1) O in *CO firstly accepts protons to generate *COH and combines with several protons to produce CH_4 by losing one water molecule [20]. (2) The protonated *CO generates *CHO and finally produces methanol through several subsequent hydrogenation processes [21].

For the reaction path of the C_2 product, the protonated *CO attached to another *CO produces *OCCOH. *OCCOH is then further protonated to form $*OCHCH_2$. The intermediate discards the O attached to the active site to generate C_2H_4 or is repeatedly hydrogenated to generate CH_3CH_2OH [22,23]. After *OCCOH discarding one water molecule, the two C atoms are attached to the active sites. Finally, CH_3COCH_3 is formed by hydrogenation and protonation. For generating C_{2+} products, the Cu, the only metal, can convert *CO to *CHO, *COH, or *OCCO, due to the suitable *CO adsorption energy, whereas Ag, Au, Fe, Ni and Pt own weaker or stronger *CO adsorption energy [24]. By constructing metal-based carbon catalysts, the electronic structures of the active center can be regulated by adjusting coordination environments such as the species and numbers of coordination atoms and metal elements [25]. For example, the Ni 3d orbital in N-doped graphene possessed an unpaired electron which could be transferred from Ni(I) to the C 2p

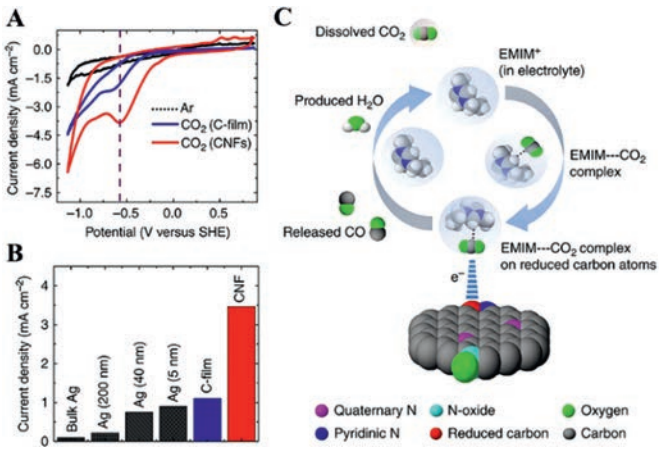

Fig. 2. (A) Cyclic voltammetry (CV) of *C*-film and CNFs in Ar or CO_2. (B) The current density of different materials. (C) Scheme of mechanism for CO_2-to-CO conversion over NCNFs. Reproduced with permission [30]. Copyright 2013, Nature.

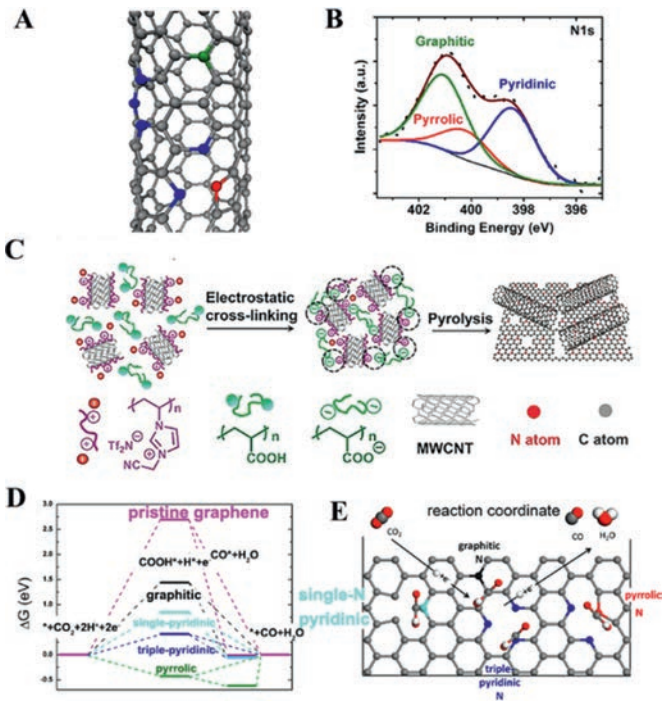

Fig. 3. (A) Schematic illustration of N configuration. (B) XPS spectrum of N 1s for NCNTs. Reproduced with permission [31]. Copyright 2015, American Chemical Society. (C) The fabrication process of HNCM/CNT [32]. Copyright 2017, Wiley-VCH. (D) Free energy diagram of the CO_2RR on NG. (E) Schematic illustration of N configuration to reduce CO_2. Reproduced with permission [35]. Copyright 2017, American Chemical Society.

orbital of CO_2 through the delocalization effect, forming the $CO_2^{\delta-}$ species to reduce the energy barrier for the CO_2RR [26].

3. Carbon-based materials for CO_2RR

3.1. Metal-free carbon materials

Carbon materials with high surface area and electronic conductivity are usually utilized as an effective matrix to load other components. Particularly, porous carbon materials can facilitate the adsorption and reduction of CO_2, as well as the rapid penetration of electrolytes due to the well-developed porosity and rich specific surface chemistry. Therefore, the structural configurations for carbon frameworks have significant influences on catalytic performance [27–29]. However, most of the metal-free carbon catalysts are electrochemically inert due to the negligible ability to activate CO_2. Thus, various strategies for the preparation of nanoporous heteroatom-doped carbon materials (*e.g.*, chemical doping and post-treatment) have been developed for the CO_2RR. For example, the incorporation of heteroatom (*e.g.*, B, N or S) can efficiently improve the electrochemical activity, because of the electronic properties effectively modulated by heteroatom doping. The tunable porous structure can increase the local CO_2 concentration through the nanoconfinement effect. The change of electronic properties arising from heteroatom doping is favorable to optimizing charge-carrier concentration, offering numerous catalytic active sites and promoting C–C coupling reactions. More importantly, the catalytic performance of carbon-based materials could be precisely tailored by the active sites within the carbon matrix.

Kumar *et al.* reported that the N-doping carbon nanofibers (NCNFs) showed about 13 times higher current density than Ag bulk for CO_2-to-CO conversion by using ionic liquids (ILs, 1-ethyl-3-methylimidazolium tetrafluoroborate) as the electrolyte (Figs. 2A and B) [30]. The ILs enabled CO_2 to form an intermediate complex (EMIM-CO_2) and thus promote the FE_{CO}, endowing NCNFs with good stability (Fig. 2C). The unchanged N 1s X-ray photoelectron spectroscopy (XPS) spectrum before and after the CO_2RR test indicated that positively charged carbon atoms were the active site rather than doping nitrogen. The redistribution of the charge and spin density of oxidized carbon atoms after doping nitrogen improved the catalytic activity of the NCNFs.

Given their unique electronic and geometric features, nitrogen-doped carbon nanotubes (NCNTs) were also employed for CO_2-to-CO conversion, showing a low overpotential of -0.18 V_{RHE} and selectivity of 80% [31]. The catalytic activity of NCNTs synthesized by the liquid chemical vapor deposition method was mainly attributed to pyridinic N which had a lone pair of electrons to bind CO_2, followed by pyrrolic and graphitic N (Figs. 3A and B). The onset potential of the pyridinic N site was -0.30 V_{RHE}, lower than that of Cu (−0.31 V_{RHE}), Au (−0.63 V_{RHE}) and Ag (−0.79 V_{RHE}), which resulted in the current density of NCNTs four times that of CNTs.

The hierarchically structured porous N-doped carbon/CNT composite membrane (HNCM/CNT) was further developed and displayed high activity, selectivity, and stability for formate with a FE of 81% (Fig. 3C) [32]. The increased pyridinic N defects in the HNCM/CNT catalyst contributed to the improvement of catalytic performance towards CO_2RR, because the basic carbon atom adjacent to the pyridinic N is prone to adsorb CO_2. Xu *et al.* further tailored nitrogen contents by adjusting the ratio of nitrogen species and the optimized catalysts showed a good selectivity of 90% for CO_2-to-CO conversion and stability of over 60 h [33]. Density functional theory (DFT) calculations illustrated that the radical anion intermediate ($CO_2^{\delta-}$) can be stabilized by N defects to lower the reduction barriers.

Compared with CNTs, graphene without interference factors (*e.g.*, curvature effects or the number of walls) can be used as a more suitable platform for an independent study of catalytic activity on different N-defect structures within the carbon network. The pyridinic N among the N-doping defects could endow adjacent carbon atoms with a positive charge. For example, N-doped graphene (NG) as a robust electrocatalyst could convert CO_2 into formate with a FE of 73% in aqueous electrolyte [34], while N-doped 3D graphene foam (NGF) displayed a good electrocatalytic performance for CO_2-to-CO conversion, rather than formate [35]. Specifically, NGF showed comparable activity with a FE_{CO} of 85% at a lower overpotential of 0.47 V, compared to Au and Ag. DFT calculations confirmed that the free energy barrier could signifi-

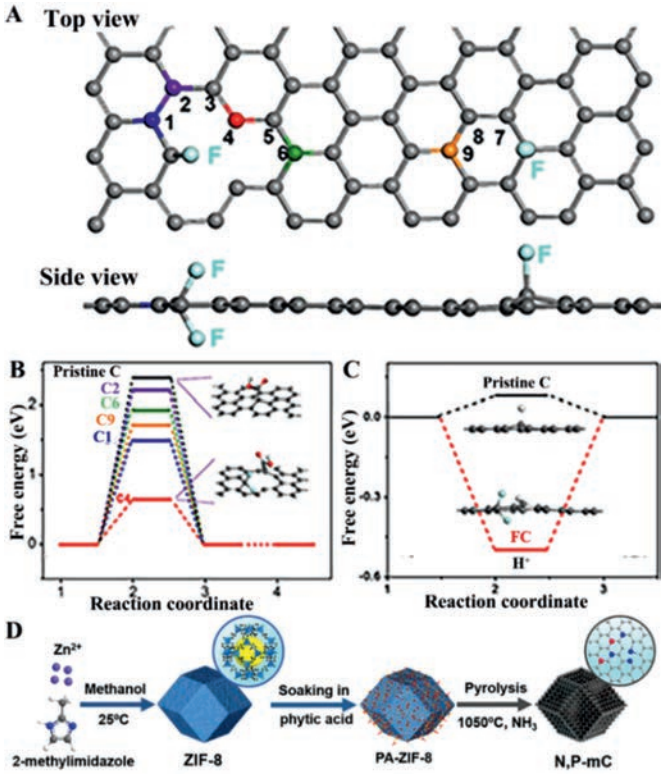

Fig. 4. (A) The different view of the DFT model for FC. (B) Free energy diagram of the CO_2RR to CO on FC and pristine C (with graphene model). (C) Schematic of the pathway on FC. Reproduced with permission [38]. Copyright 2018, Wiley-VCH. (D) Fabrication scheme of N, P-mC. Reproduced with permission [39]. Copyright 2021, Wiley-VCH.

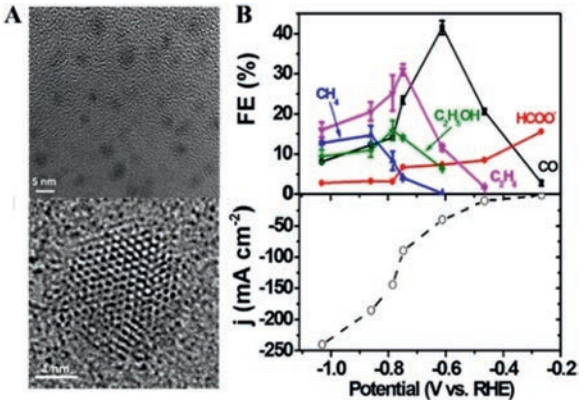

Fig. 5. (A) TEM (TOP) and high-resolution TEM for N-doped carbon-based materials. (B) FE of different products and the current density of NGQDs. Reproduced with permission [43]. Copyright 2017, American Chemical Society.

cantly decrease after adding N atoms in graphene owing to triple-pyridinic N strongly binding intermediate COOH* (Figs. 3D and E).

Considering the porous structure and chemical diversity on the surface, the nanoporous carbon (NPC) materials are also excellent electrocatalysts for the CO_2RR. Yang *et al.* reported that the structure of carbon nanofiber membranes can be tuned by co-doping N and S and constructing hierarchical pores [36]. The as-synthesized membranes with excellent flexible and free-standing properties exhibited a FE_{CO} of 94% at a current density of 103 mA/cm^2. Besides, Se-doped carbon nanosheets (Se-CNs) with different sizes of the porous structure were also designed for the CO_2RR [37]. Impressively, Se-CNs with the optimized active sites, high surface area, and hierarchical pores, were able to promote penetration, transport, and the reaction of the reactants, and thus the partial current density of CO for Se-CNs was over 11 times that of CNs. Through edge-Se-C-N-configurations obtained by XPS and extended X-ray absorption fine structure (EXAFS) analysis, Se-CNs catalyst exhibited a smaller free energy barrier (0.32 eV) than that of CNs (0.63 eV), the proper adjustment of electronic structures made the electronic state of the active site more suitable for bonding CO_2 rather than adsorbing hydrogen. Accordingly, Se-CNs displayed better selectivity of CO (90%).

Fluorine-doped carbon (FC) by pyrolyzing commercial BP2000 with a fluorine source can also achieve a highly selective CO_2-to-CO conversion with a FE of 89.6% and a small Tafel slope of 81 mV/dec [38]. DFT calculations revealed that C4 and C9 located on the metal position of FC possessed the low Gibbs free energy barrier, conducive to COOH* adsorption (Figs. 4A–C). Furthermore, Kuang *et al.* applied a second doping process to increase the density of pyridinic N and defects after pyrolysis of ZIF-8, achieving a good FE_{CO} of 92% [39]. Subsequently, Pan *et al.* achieving N, P-co-doping mesoporous carbon (N, P-mC) by annealing phytic-acid-functionalized ZIF-8 in NH_3 and the obtained materials achieved selectivity close to 100% (Fig. 4D) [40].

N-Doped carbon can effectively enhance the activity of quantum dots towards CO_2RR [41,42]. For example, Ajayan and co-workers reported that N-doped graphene quantum dots (NGQDs) with an abundant density of N-doping defects could be prepared by exfoliating N-doped graphene oxide (GO) (Fig. 5A) [43]. Interestingly, different species could be regulated by potential on NGQDs, ranging from single-carbon to multi-carbon products. Local density of states and thermodynamic free energy of intermediate states further confirmed that N-doped GQD and CNT showed a much larger energy gain compared to NG, contributing to binding *COOH to achieve a high catalytic activity (Fig. 5B). Owing to the easy, inexpensive and large quantity production and earth-abundance, graphene-like carbon nitride (g-C_3N_4) with abundant pyridinic nitrogen species is a promising candidate for heterogeneous catalysis [44]. Lu *et al.* constructed graphitic carbon nitride onto multiwall carbon nanotubes (g-C_3N_4/MWCNTs) by treating the precursor (dicyandiamide and MWCNT) in a H_2SO_4 and HNO_3 mixture (3:1, v/v) and polycondensation, and the g-C_3N_4/MWCNTs with covalent attachment achieved a maximum FE_{CO} of 60% and prominent stability of 60 h [45]. This work revealed that the electronic structures of g-C_3N_4 can be effectively modified by metal-free carbon materials. Subsequently, Zhi *et al.* reported that g-C_3N_4/doped graphene materials could significantly boost CO_2 reduction *via* the interfacial electron transfer [46]. With the assistance of computational methods, the impact of heteroatom doping (X = B, N, O, P) was comprehensively explored. The observed variable adsorption energetics and electronic structures, among different doping cases, indicated that the interfacial electron transfer modulation can promote the catalytic performance for producing methane.

In addition to conventional CNT and graphene structures, diamond nanocrystals with unique tetrahedral bonding units can facilitate C–C coupling. Although the electrical conductivity of pristine diamonds is poor, it can be substantially promoted by doping. Through microwave plasma-enhanced chemical vapor deposition, Liu *et al.* deposited N-doped nanodiamond (NDD) on Si rod array substrates, achieving a high FE of 77.6% towards CH_3COOH and improving the selectivity for C_{2+} products (Figs. 6A–C) [47]. Afterward, the same group further applied a hot filament chemical vapor deposition method to achieve B and N element co-doped nanodiamond (BND) [48]. The obtained materials can achieve a FE of 93.2% towards C_2H_5OH (Fig. 6D), owing to the synergistic effect between B and N on BND.

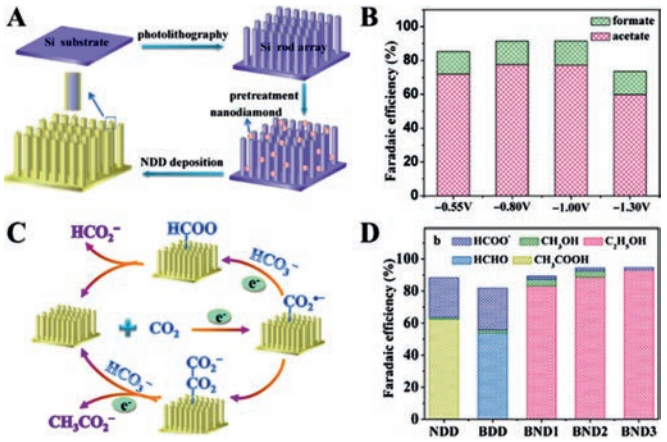

Fig. 6. (A) Scheme of fabrication of NDD/Si rod array. (B) FE of different products. (C) The reaction pathways for NDD/Si rod array. Reproduced with permission [47]. Copyright 2015, American Chemical Society. (D) FE for the different percentages of N in NDD materials. Reproduced with permission [48]. Copyright 2017, Wiley-VCH.

3.2. Metal-based carbon materials

Anchoring metal on carbon composite is an ideal strategy for large-scale production. The synergistic effect between metals and carbon materials contributed to improving catalytic activity and selectivity towards specific products, where the metal elements (Au, Pd, Ag, Fe, Co, Ni, Cu, In, *etc.*) can efficiently adsorb and activate CO_2 to lower the energy barrier, and carbon materials with the high surface areas and tunable porous structure supply a large electrochemical active area to decrease the diffusion resistance [49–53]. As known, Cu is regarded as the fundamental metal for electrocatalytically converting CO_2 into multi-carbon products. The strong defect sites within carbon-supported Cu catalysts can stabilize related intermediates and alter the selectivity of the catalyst for specific products. Generally, HOCCH* is a key intermediate that determines whether the product is ethylene or ethanol. Gangeri *et al.* investigated the conversion of CO_2 into various oxygenates by coating Fe or Pt onto CNT (Fe/CNT or Pt/CNT) [54]. Although Fe/CNT exhibited better catalytic activity than Pt/CNT, the faster deactivation occurred on Fe/CNT due to the cross-over of the electrolyte, particularly K ions. It was found that FeO_x compounds were produced on the CNTs after reaction. Furthermore, Wang *et al.* investigated the confinement effect using amorphous N-doped carbon/Cu (N–C/Cu) to improve the selectivity for C_2H_5OH (52% ± 1%) [55]. The capping layers (N–C) possessed a strong electron-donating ability, which can effectively promote C–C coupling and suppress the deoxygenation process to achieve an enhanced selectivity for ethanol. Zhong *et al.* also constructed Fe and N doped porous carbon nematosphere (FeNPCN) for the CO_2-to-CO conversion, exhibiting a high FE_{CO} of 94% [56]. 3D hierarchical FeNPCN was prepared by carbonizing FeO-PDA formed by the polymerization of dopamine triggered by Fe species. The addition of the Fe atom can effectively promote the formation of the intermediates because Fe-N coordination is conducive to the formation of the COOH* intermediate. Moreover, the composition of the syngas, *i.e.*, the ratio of CO and H_2, could be efficiently adjusted. Similarly, Sun *et al.* integrated bismuth and bismuth oxide nanoparticles (NPs) on nitrogen-doped reduced graphene oxide nanosheets (Bi/Bi_2O_3/NrGO) by combining the hydrothermal method and calcination [57]. The strong synergistic effect between Bi and Bi_2O_3 together with the undercoordinated sites efficiently improved the catalytic performance, which achieved a FE of 85% for formate with a low Tafel slope of 166 mV/dec. Besides, Du *et al.* integrated CoO on N-doped mesoporous carbon and carbon nanotubes (MC–CNT/Co) for reducing CO_2 to CH_3CHO and C_2H_5OH [58]. The pyrrolic-N and pyridinic-N on MC–CNT can significantly promote the C–C coupling and stabilize *CO generated by CoO, which is favorable to forming C_2H_5OH. Superior to other N-containing carbon substrates, the g-C_3N_4 with abundant pyridinic nitrogen atoms can efficiently contact with oxygen-bound intermediates (*OCH_x, *O and *OH) thanks to high affinity, contributing to the deep reduction of CO_2. For example, the g-C_3N_4 as a molecular scaffold can appropriately modify the electronic structure of Cu, which could optimize some key reaction intermediates (Figs. 7A and B) [59]. Interestingly, Cu-C_3N_4 with the strong adsorption of CO contributed to the lower free energy level for the intermediates (Figs. 7C and D). Thus, the Cu-C_3N_4 surface can greatly benefit the activation of CO_2, leading to a more facile reaction to desirable products, compared to the Cu(111) surface and other Cu complexes on nitrogen-doped carbons. Afterward, g-C_3N_4 supported Au NPs was synthesized by Zhang *et al.*, achieving a FE_{CO} of over 90% in a wide range of potential from −0.45 V_{RHE} to −0.85 V_{RHE} [60]. Impressively, the negatively charged Au surface induced by the interaction of two compounds could stabilize the key intermediate *COOH to enhance the CO_2RR performance, further confirmed by the DFT. (Figs. 7E-G).

To date, the engineering of defect, interface, strain, lateral size and thickness, and heteroatom doping have been considered as effective approaches to improve the catalytic activity of 2D materials [61,62]. Interestingly, downsizing the metal NPs to single-atom level, single-atom catalysts (SACs) with unique electronic structure, low-coordinated metal atoms, strong metal-support interactions, and maximum atom utilization can integrate the advantages of both homogeneous and heterogeneous catalysts [63–66]. SACs with isolated metal atoms dispersed on conductive support have shown excellent catalytic performance and thus become a research hot in the field of catalysis [67–69]. Combining atomically dispersed metal sites and the coordinated atoms can greatly boost the catalytic performance towards CO_2RR by facilitating the activation or the dissociation of the intermediates [70–73]. More importantly, the fabrication of SACs contributes to systematically understanding the underlying relationship between material structure and properties at atomic level [74]. Physical adsorption, polymerization, chemical bonding, or integration in frameworks endowed complexes with well-defined metal-N_x (M-N_x) sites. SACs with M-N_4 sites as the efficient electrocatalysts for the CO_2RR were confirmed by DFT calculations [75–80]. To obtain heterogeneous catalysts with atomically dispersed metal sites, a common method is to pyrolyze metal precursors using appropriate nitrogen and carbon sources [81]. In 2015, Strasser *et al.* prepared N-doped porous carbon black (N–C) containing different metals by repeated heat treatments and acid-leaching processes [82]. They found that the N–C catalyst presented a similar selectivity to the N-doped carbon catalysts with M-N_4 moieties. More importantly, the metal sites could further reduce the adsorbed CO to hydrocarbons. Through a topo-chemical, catalyst with an exclusive Ni-N_4–C structure can accelerate charge transfer and lower free energy to form *COOH [83]. Atomic Fe dispersed on N-doped graphene catalysts with Fe-N_4 moieties showed a high FE_{CO} of over 90% in a flow cell reactor at low overpotential due to the high CO_2 adsorption and CO desorption of discrete Fe^{3+} ions coordinated with pyrrolic N atoms [84]. In 2020, Zhang and co-workers applied a feasible strategy to synthesize the In single-atom catalyst (In-SAs/NC) with exclusive isolated In-N_4 atomic interface sites for generating formate [85]. By combining a wet-impregnation process and pyrolysis process, the main group of indium catalysts can be accurately regulated at the atomic scale. Therefore, catalyst displayed a large turnover frequency (TOF) of 12,500 h^{-1} at 0.95 V_{RHE}, and the FE for formate and current density could reach 96%, 8.87 mA/cm^2, respectively.

The coordinated N ligands act as a crucial role in improving the catalytic performance of SACs towards CO_2RR. The surface-active

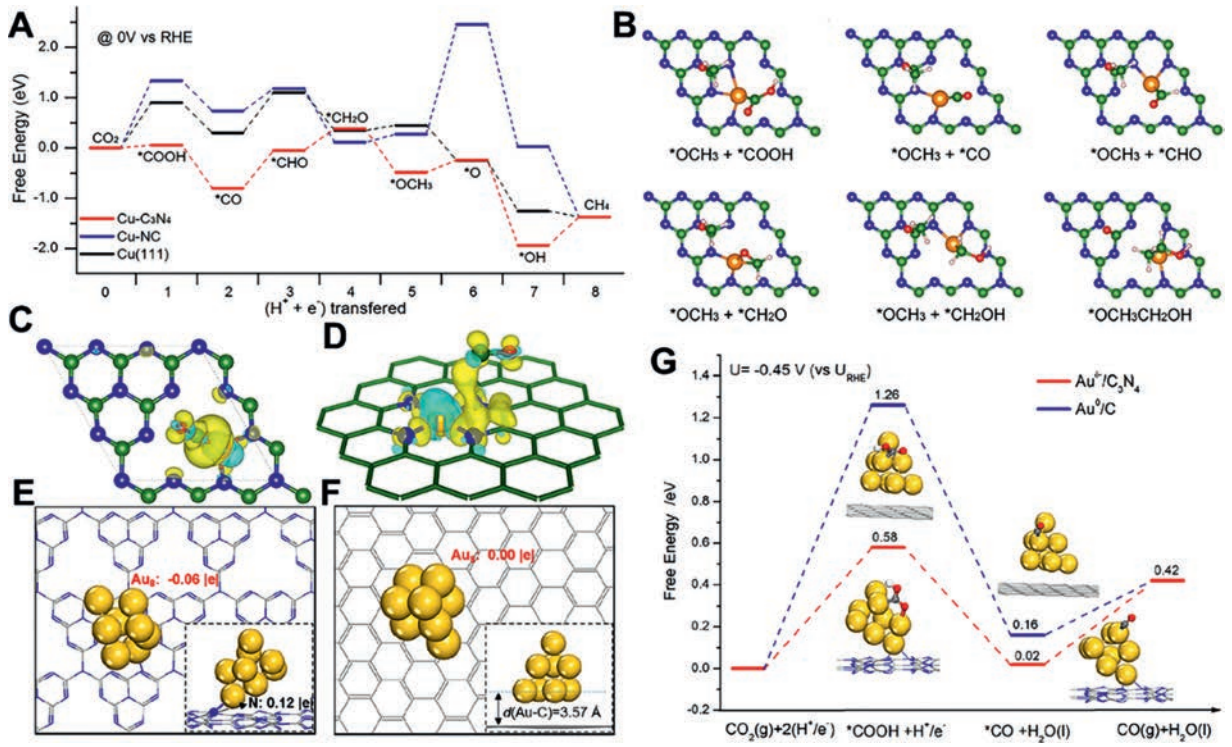

Fig. 7. (A) The reaction pathways for Cu-C_3N_4. (B) The main reaction intermediates for producing CH_3CH_2OH on Cu-C_3N_4. The electron density for CO adsorbed on (C) Cu-C_3N_4 and (D) Cu-NC. Reproduced with permission [59]. Copyright 2017, American Chemical Society. Au_8 cluster adsorbed on C_3N_4 (E) at the hollow site and (F) at the graphene-carbon support. (G) The Gibbs free-energy diagram for $Au^{\delta-}/C_3N_4$. Reproduced with permission [60]. Copyright 2018, American Chemical Society.

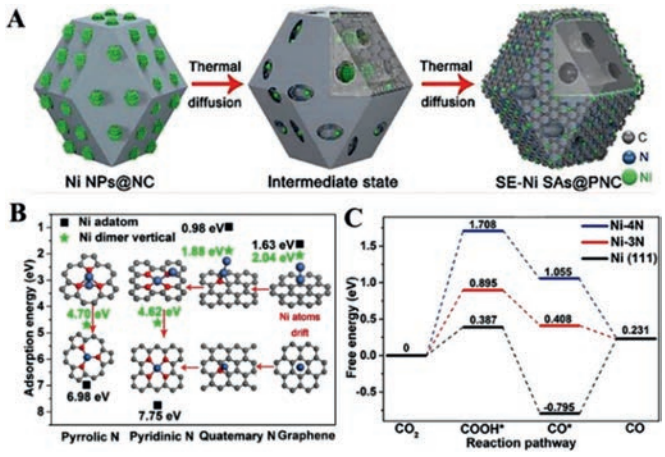

Fig. 8. (A) The scheme of the transformation of Ni NPs into Ni SAs. (B) Adsorption energies of the Ni active site. (C) Free-energy diagram for the CO_2-to-CO conversion. Reproduced with permission [86]. Copyright 2018, Wiley-VCH.

sites can effectively suppress mass transfer and improve the atom economy. The supported Ni metal NPs can be transformed to thermal stable Ni single atoms that were mostly located on the surface of pyrolysis-treated ZIF-8 as the support, through thermal atomization (SE-Ni SAs@PNC) (Fig. 8A) [86]. When Ni nanoparticles contacted with N-doped carbon with abundant defects, this synthetic process not only transformed the Ni NPs into single atoms owing to the strong coordination and the continuous loss of atomic Ni species, but also created numerous pores to facilitate the contact of dissolved CO_2 and single Ni sites. Moreover, carbon substrate can stabilize the surface of atomization of Ni NPs. The contrast experiment that Ni NPs dispersed on the non-defective XC-72 matrix without any aggregation occurred the migration and aggregation of Ni atoms after a pyrolysis treatment revealed that the defective NC is a crucial factor for the formation of the SAs. Compared to pyridinic N-coordinated Ni (Ni-4N), pyrrolic N-coordinated Ni (Ni-3N) possessed lower free energy for *COOH intermediate. Pyrrolic N-coordinated atomically dispersed metal ions also presented more outstanding activity and stability than pyridinic N-coordinated catalysts (Figs. 8B and C). Besides, anchoring atomically dispersed Co-N_5 structure on polymer-derived hollow N-doped porous carbon spheres was also designed to implement a robust CO_2RR [87]. The X-ray absorption near-edge structure (XANES) and EXAFS revealed that a single Co atom possessed a positive charge and the valence of the Co element in the obtained catalyst was slightly higher than that of CoPc. Interestingly, the Co-N_5 sites were the active center and played a crucial role in the rapid formation of COOH* intermediate and the desorption of CO.

Strasser *et al.* designed a series of M-N-C *via* an impregnation process and subsequent heat treatments (Fig. 9A) [88]. Specifically, the obtained Ni-N-C catalyst exhibited better catalytic performance, followed by Fe-N-C catalyst (Figs. 9B and C). This result was further confirmed by Li *et al.* (Figs. 9D and E) [78]. The ultrathin graphene-like Ni-N-C catalysts *via* pace-confinement-assisted molecular-level complexing approach achieved the highest FE_{CO} of 96% and the TOF of 1060 h^{-1} at a moderate overpotential, compared to other M-N-C catalysts (M = Mn, Co, Fe, Cu, *etc.*). Besides, Pan *et al.* confined low-valent Ni-based NPs within nitrogen-doped carbon (Ni-NC) catalyst for the CO_2RR, exhibiting a maximum FE_{CO} of 98% [89]. Interestingly, Ke and co-workers synthesized a highly active manganese N-heterocyclic carbene pincer complex ([MnCNCOMe]BF_4) [90]. The strong electron-donating ability of the -OMe group and electronic tuning by para substitutions are favorable to the conversion of CO_2 into CO.

Metal-organic frameworks (MOFs) are porous hybrid materials consisting of metal nodes and organic ligands [91–94]. The active sites within a particular metal-ligand periodic interval of MOFs are

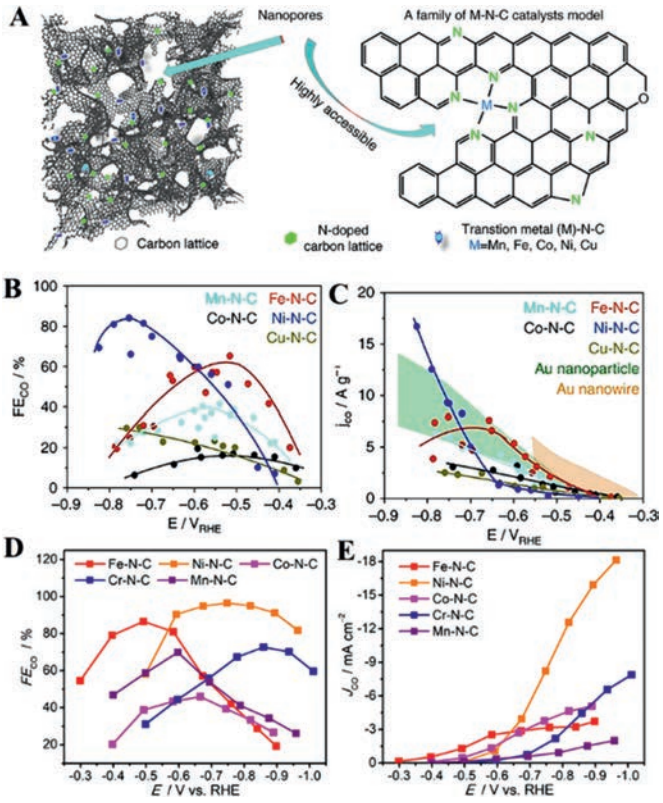

Fig. 9. (A) Materials model and a schematic local structure. (B) FE_{CO} of different catalysts. (C) Catalyst mass-normalized CO partial currents of different catalysts. Reproduced with permission [87]. Copyright 2017, Springer Nature. (D) FE_{CO} of different structures. (E) Catalyst mass-normalized CO partial currents of different structures. Reproduced with permission [78]. Copyright 2018, Elsevier.

in a state of monoatomic dispersion. Pristine MOFs can be used as electrocatalyst precursors or templates to fabricate MOF-derived porous carbon nanomaterials with superior conductivity and stability. Inspired by electrocatalytic degradation of carbon tetrachloride by Co-porphyrinic MOF [95], Kubiak's group applied electrophoretic deposition to construct a heterogeneous system by integrating redox-conductive Fe-porphyrins into thin MOF-525 films, which electrochemically covered catalytic sites ($\sim 10^{15}$ sites/cm^2) in conductive surface [96]. The active Fe(0)-porphyrin species in Fe-based MOF films can produce 15.3 μmol/cm^2 of CO and 14.9 μmol/cm^2 of H_2, whose current density can reach 2.3 mA/cm^2 within 0.5 h, and turnover number (TON) for CO in controlled potential electrolysis (CPE) was 272. With an acidic proton donor (trifluoroethanol, TFE), the TON of Fe(0)-porphyrin system reached 1520. Moreover, the current density and stability were up to 5.9 mA/cm^2 and 3.2 h, respectively, better than that without TFE.

Whereafter, Albo *et al.* further investigated the electrocatalytic reduction of CO_2 by using MOFs (HKUST-1, CuAdeAce) and metal-organic aerogels (CuDTA, CuZnDTA) [97]. By cyclic voltammograms (CV), HKUST-1 showed the best current density after five scans among the above-mentioned four materials, indicating an excellent performance in transferring electrons. The HKUST-1 with a surface area of 1710 m^2/g exhibited maximum yield rates of 5.62×10^{-6} and 5.28×10^{-6} mol m^{-2} s^{-1} for CH_3OH and C_2H_5OH, respectively. Because the charge can be transported within MOF films by either linker or electron/hole redox hopping. 3D porphyrin-based MOF-525 catalyst synthesized by dip-coating method admirably converted CO_2 into CO with low overpotential, achieving a maximum FE_{CO} of 91% and a TOF of 0.336 site^{-1} s^{-1} after 10 h electrolysis [98]. Liu *et al.* applied epitaxially-grown molecular ($ReL(CO)_3Cl$) to surface-grafted MOF catalyst, and monolithic coatings obtained

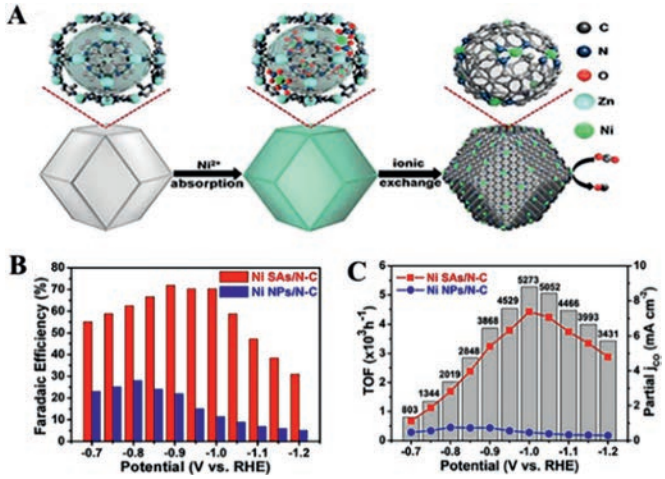

Fig. 10. (A) Illustration of the synthesis process of Ni SAs/N–C. (B) FEs of CO. (C) TOF and partial CO current density. Reprinted with permission [102]. Copyright 2017, American Chemical Society.

current densities exceed 2 mA/cm^2 with a FE_{CO} of 93% [99]. Due to the porosity and conformance of the inherited catalytic active sites after carbonization, MOF was a potential candidate in the field of non-noble metal catalysts. Zhao *et al.* synthesized OD Cu/C catalysts by the pyrolysis of HKUST-1 to convert CO_2 into ethanol [100]. The carbon matrix can protect Cu from deactivation and improve the efficient transfer of CO_2 and diffusion of the products to the solutions. The synergetic effect of the highly dispersed Cu and C matrix rendered the production rate for the methanol and ethanol up to 12.4 and 13.4 mg L^{-1} h^{-1}, respectively, with a total FE of 71.2% at -0.3 V_{RHE}. In addition, the metal-metal interface plays an important role in improving the activity and selectivity of the catalysts. Three heterometallic HKUST-1 dopped ions (Zn, Ru, Pd) reported by Albo *et al.* were also applied to investigate the catalytic performance towards CO_2RR [101]. Ru(III)-electrocatalyst showed the highest yield of alcohol (47.2%).

Wu's group prepared nitrogen-doped porous carbon by ZIF-assisted strategy and ionic exchange, where Ni ions were utilized to replace Zn within the cavities of ZIF-8 (Ni SAs/N–C) (Fig. 10A) [102]. Due to the improved adsorption energy towards CO and electronic conductivity, the electron can rapidly shift from the electrode to the absorbed CO_2 to form a radical intermediate. Thus, the Ni SAs/N–C displayed a FE_{CO} of over 71.9% with a prominent TOF of 5273 h^{-1} and the current density can reach 10.48 mA/cm^2 (Figs. 10B and C). Based on the gas diffusion electrode (GDE), Li's group applied $Cu_3(BTC)_2$ to capture CO_2 for synthesizing hydrocarbons, in which capture capacity reached up to 1.8 mmol/g [103]. Under relatively negative potentials, the FE of CH_4 for $Cu_3(BTC)_2$ can double without the addition of $Cu_3(BTC)_2$. While for the competitive HER, the FE of H_2 was declined to 30%.

Yang *et al.* employed a multi-step pyrolysis approach to fabricate atomically dispersed transition metals (Ni, Co, NiCo, CoFe and NiPt) on N–CNTs (NiSA-N-CNTs) for the CO_2-to-CO conversion [104]. The obtained materials were subsequently characterized by aberration-corrected scanning transmission electron microscopy and X-ray absorption spectroscopy (XAS) to explore the coordination structures. While pyridinic N and graphitic N kept the same in *ex situ* XANES spectroscopy, Ni L-edge peak revealed higher photon energy, revealing that Ni-N species were the active centers for the CO_2RR. The NiSA-N-CNTs can achieve a high FE_{CO} of 91.3% and a TOF of 11.7 s^{-1}. It has been confirmed that the Ni-N_4–C structure can exhibit excellent catalytic activity towards the CO_2RR. Recently, low-coordination single-atom Ni electrocatalysts (Ni-N_3–C) were obtained *via* a facile post-synthetic metal substitution (PSMS)

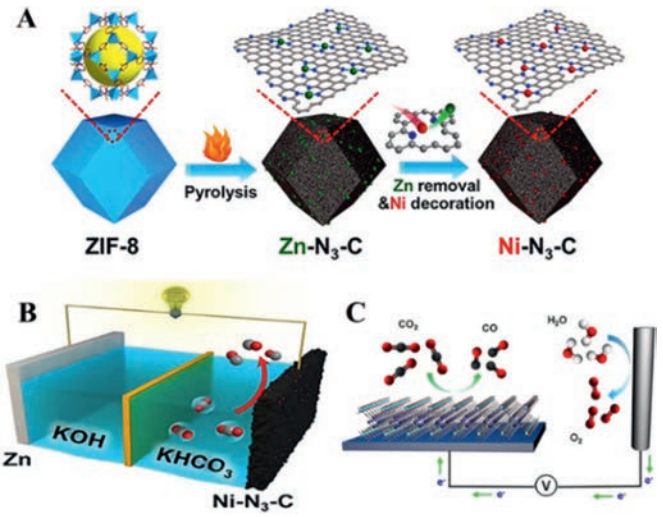

Fig. 11. (A) Scheme of fabrication of Ni-N_3–C catalyst. (B) The scheme of Zn-CO_2 battery using Ni-N_3-C as cathode catalyst. Reprinted with permission [101]. Copyright 2021, Wiley-VCH. (C) The scheme of TCPP-Co with Al-based MOF for the CO_2RR. Reprinted with permission [106]. Copyright 2017, American Chemical Society.

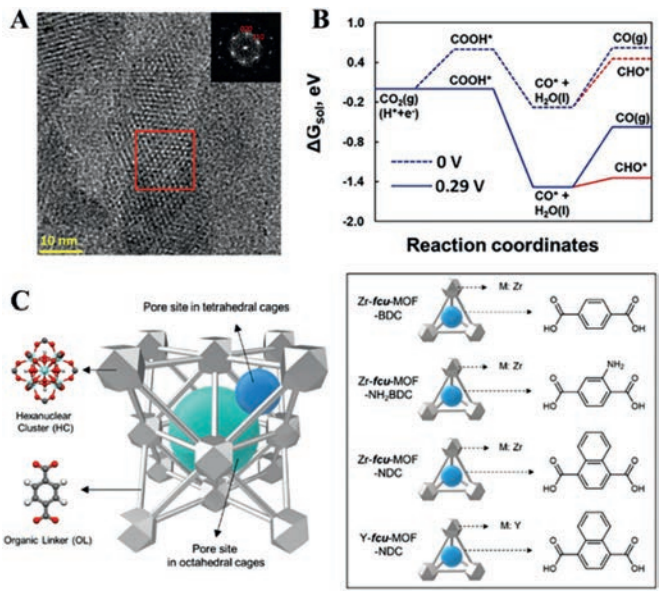

Fig. 12. (A) HRTEM and Fourier transform of Cu-THQ. (B) The free energies of Cu-THQ. Reproduced with permission [111]. Copyright 2021, Wiley-VCH. (C) The synthesized design strategies of MOF. Reproduced with permission [114]. Copyright 2021, American Chemical Society.

strategy [105]. After the pyrolysis of the Zn-MOF, acid treatment and decoration, abundant Ni-N_3 sites were formed (Fig. 11A). Importantly, Ni-N_3–C catalyst showed better catalytic performance than Ni-N_4–C and N–C owing to the favorable kinetics. This result was also confirmed by XPS spectrum, synchrotron-based XAS measurement and Fourier transforms (FT) extended X-ray absorption fine structure. Ni-N_3–C catalyst with a high TOF of 1425 h^{-1} can be used in the Zn-CO_2 battery, showing a discharge potential of 0.41 V (Fig. 11B). Moreover, integrating MOF with the function of support for electrochemical CO_2-to-CO conversion is an intriguing strategy, which is capable of tailoring active molecular in the porous network to maximize active sites. The charge transport could be controlled by the morphology of MOF. Yaghi *et al.* incorporated the active molecule (TCPP-Co) into an Al-based MOF (Fig. 11C) [106]. They found that all of the active sites in homogeneous catalysts (porphyrin molecular) can contact the electrolyte, electrons and their transfer can be changed by adjusting the morphology and thickness of MOF. The selectivity for CO was over 76% at −0.7 V_{RHE}, running for over 7 h.

Further, a NC/MOF hybrid comprising Ag NCs thin film (Ag@Al-PMOF) was constructed to improve the performance towards CO_2RR and suppress HER [107]. The change of the interface between the NPs and the MOFs can not only change the electronic structure of Ag but also contribute to suppressing HER and promoting the CO_2RR, compared to the bare Ag NC counterparts. In 2019, Zhang and co-workers fabricated exclusive Bi-N_4 sites on porous N-doped carbon networks (Bi SAs/NC) through thermal decomposition of the Bi-MOF and dicyandiamide (DCD) [108]. The synthesized complex achieved high activity for CO_2-to-CO conversion with a high FE_{CO} of 97% and a TOF of 5535 h^{-1}. Compared with the Bi clusters or nanoparticles, the Bi atoms achieved a higher FE of CO. It is worth noting that Bi is regarded as the material for generating formate, while BiN_4/C with a low free energy barrier is conducive to the formation of CO.

Owing to the intrinsically electrically insulated property, pristine MOFs have been rarely studied in electrocatalysis. Recently, the electrical conductive MOFs have been constructed *via* through-bond approach, extended conjugation approach, through-space approach, guest-promoted approach, and so on [109,110]. The enhanced electrical conductivity can endow MOFs with excellent catalytic performance and provide a new pathway to boost the development of the CO_2RR. For example, 2D Cu-based conductive MOF (copper tetrahydroxyquinone, Cu-THQ) was constructed for the CO_2RR and achieved a FE_{CO} of 91% at a high current density of 173 mA/cm^2, which are more active than other reported MOFs-based catalysts [111,112]. The HRTEM images illustrated that Cu-THQ displayed a honeycomb arrangement with the AB stacking model (Fig. 12A). The operando Cu K-edge X-ray absorption near-edge spectroscopy and DFT calculations revealed the existence of reduced Cu (Cu^+) and Cu-THQ with the CO adsorption free energies was favorable to converting CO_2 into CO (Fig. 12B). Meanwhile, 2D Cu-THQ with high atomic utilization and easy surface modification contributed to the improvement of performance [113]. Sargent *et al.* systematically incorporated Ag NPs in face-centered cubic MOFs which was changed by modifying both the organic linker (1,4-benzene dicarboxylic acid, BDC, and 1,4-naphthalenedicarboxylic acid, NDC) and the metal node (Zr and Y), improving the FE_{CO} from 74% to 94% (Fig. 12C) [114]. The advanced technologies can contribute to the deep investigation of the mechanism reaction. In this work, XAS and *in situ* Raman spectroscopy confirmed that the surface of Ag NPs in stable MOFs can effectively optimize the *CO binding mode by increasing local CO_2 concentration, achieving CO_{atop}/CO_{bridge} control, rather than conventionally controlling the binding energy.

To avoid the energy penalty, tandem catalysis has been considered as an efficient strategy to generate high-value products (C_{2+}) [115]. For example, Sargent *et al.* integrated FeTPP[Cl] (5,10,15,20-tetraphenyl-21*H*,23*H*-porphine iron(III) chloride) on a sputtered Cu electrode (FeTPP[Cl]/Cu) to investigate the molecule-metal interfaces [116]. FeTPP[Cl] sites showed excellent catalytic activity for *CO, leading to the increased concentration of CO near the Cu surface, which can lower reaction energy for *CHCHOH to steer selectivity from C_2H_4 to C_2H_6OH (41%).

Formate is an important chemical raw material, and many researchers focus on improving the performance of Bi-based, In-based, and Sn-based catalysts for the conversion of CO_2 into formate. Bi-based catalysts are regarded as the most commercially available materials for producing formate [117]. In 2020, Zhu *et al.* firstly obtained atomically thin bismuthene (Bi-ene) by *in situ* electrochemically transforming Bi-based metal-organic layers (Fig. 13A)

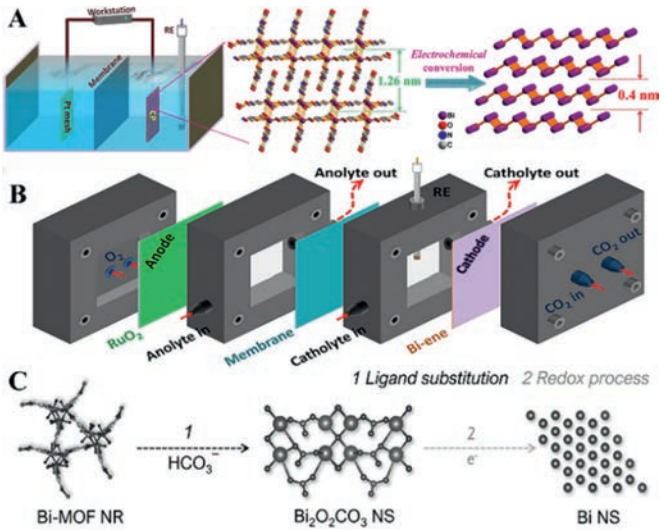

Fig. 13. (A) The scheme of synthesis of Bi-ene. (B) Illustration of the self-designed flow cell. Reprinted with permission [118]. Copyright 2020, Wiley-VCH. C) Diagram of reconstruction of Bi-MOF. Reprinted with permission [124]. Copyright 2021, Wiley-VCH.

[118]. Interestingly, *in situ* attenuated total reflection-infrared spectroscopy (*in situ* ATR-IR) indicated that the adsorbed HCO_3^- groups participated in the first proton-couple electron transfer process during the CO_2RR, which was consistent with the analysis of the Tafel test and DFT. The obtained Bi-ene in a flow cell reactor can achieve nearly full conversion for formate in a wider potential range and different electrolytes (Fig. 13B). Furthermore, Bi(1,3,5-tris(4-carboxyphenyl)benzene) (Bi(btb)) as the precatalyst underwent a structural rearrangement upon electrocatalysis to produce Bi crystalline, achieving a FE of 95% towards formate [119]. Similar results were also reported in previous literature [120–123]. Relying on the Bi element, these reports achieved a high FE for the formate, but the structure change of Bi-based MOFs during the reaction process remains unclear.

In 2021, Qiao *et al.* monitored and controlled the reconstruction of a Bi-based MOF during the electrochemical CO_2 reduction (Fig. 13C) [124]. They found that Bi-based MOF was firstly converted into $Bi_2O_2CO_3$ in electrolyte and then $Bi_2O_2CO_3$ was mediated to Bi by applying potential. Bi catalysts after intentionally reconstructed exhibited high activity, excellent selectivity, and long-term durability for generating formate. This work indicates the significant impact of pre-catalyst reconstruction during the reaction and provides a pathway for the rational design of highly active and stable electrocatalysts.

4. Conclusions and perspective

The electrochemical reduction of CO_2 has been considered as one of the most promising approaches to close the carbon cycle, solve environmental issues and meet energy demands. Until now, various carbon-based catalysts including graphene, carbon nanotubes, quantum dots, porous carbon, and MOF-based catalysts have been fabricated, exhibiting good FEs and selectivity towards the CO_2RR. Due to the tailorable porous structures, abundant resources, and excellent catalytic properties, carbon-based materials are efficient in the reduction of CO_2 to the value-added carbon products. The relevant experiments have been completed, as shown in Table 2. Concerning metal-based carbon catalysts, improving the utilization efficiency of metal atoms is of essential significance for reducing the catalyst cost and promoting sustainability. Through a combination of experiment and theory, precisely controlling the structure of metal-based carbon composite catalysts provides an enormous opportunity for investigating the relationship between structure and performance.

Despite these promising achievements, the catalytic performance still needs to be improved especially in terms of current densities, FE, and selectivity. The catalytic performance of carbon-based catalysts depends on the surrounding environment, active sites, and physicochemical properties. Besides, the multiple electron pathways of the CO_2RR (even more than 18-electron) would generate various related intermediates which can provide many arrangements for protonation, leading to the complexity of the product and uncontrollable process. Furthermore, more efforts are needed to further direct a deeper understanding of the catalytic process to find the optimal catalyst and reaction conditions. Therefore, for the in-depth understanding of possible pathways for the key intermediates and structure-activity relationships, various ad-

Table 2
The performance of different MOFs and their related products in the CO_2RR.

	Material	Main product	Electrolyte	Faradaic efficiency (%)	Current density (mA/cm^2)	Potential (V, *vs.* RHE)	Ref.
Metal-free carbon materials	NCNFs	CO	EMIM-BF_4	98		−0.573	[30]
	NCNTs	CO	0.1 mol/L $KHCO_3$	80	1.0	−0.26	[31]
	HNCM/CNT	formate	0.1 mol/L $KHCO_3$	81		−0.8	[32]
	NGF	CO	0.1 mol/L $KHCO_3$	85	1.8	−0.47	[35]
	NG	formate	0.5 mol/L $KHCO_3$	73	7.5	−0.84	[34]
	NSHCF	CO	0.1 mol/L $KHCO_3$	94	103	−0.7	[37]
	FC	CO	0.1 mol/L $NaClO_4$	89.6	0.24	−0.62	[38]
	NGQD	C_2H_4	1 mol/L KOH	31	100	−0.75	[43]
	NDD/Si RA	CH_3COOH	0.5 mol/L $NaHCO_3$	77.3–77.6		−0.8∼1.0	[47]
	BND	ethanol	0.1 mol/L $NaHCO_3$	93.2		−1.0	[48]
Metal-based carbon materials	N-C/Cu	ethanol	1 mol/L KOH	52 ± 1	156 ± 3	−0.68	[55]
	Fe^{3+}–N–C	CO	0.1 mol/L $KHCO_3$	over 90	94	−0.45	[84]
	SE-Ni SAs@PNC	CO	0.5 mol/L $NaHCO_3$	87.8	18.3	−1.0	[86]
	Ni–N–C catalysts	CO	0.1 mol/L $KHCO_3$	85		−0.78	[88]
	NiSA-N-CNTs	CO	0.5 mol/L $NaHCO_3$	91.3	23.5	−0.7	[104]
	$Al_2(OH)_2$TCPP-Co	CO	aqueous bicarbonate buffer	76		−0.7	[106]
	Bi SAs/NC	CO	0.1 mol/L $NaHCO_3$	97	5.1	−0.5	[108]
	Cu-THQ	CO	1 mol/L choline chloride and 1 mol/L KOH	91	173	−0.135∼0.43	[111]
	Bi-ene	formate	0.5 mol/L $KHCO_3$	close to 100	72.04	−0.83∼1.18	[118]
	Bi-based MOFs	formate	0.1 mol/L $KHCO_3$	92	15	−1.1	[124]

vanced *in situ* characterization technologies, such as *operando* XAS, *in situ* Raman spectroscopy, electron paramagnetic resonance, *in situ* surface-enhanced infrared absorption spectroscopy, *in situ* ATR-IR, and *in situ* XPS should be further developed and adopted to detect electrochemical reaction or monitor the change of surface state and atomic structure. An electrocatalytic microdevice of the CO_2RR like the chip should also be constructed to directly probe dynamic changes of the catalyst or electrochemical processes.

Identifying the specific role of each component involved in multiple carbon-based composites towards the CO_2RR is a great challenge. In this regard, some new measures or approaches should be further taken to achieve this goal. For example, fabricating conductive MOF *via* doping, ligands decoration, is a proper strategy for improving the performance of carbon-based catalysts. In addition, fabricating carbon-based tandem catalysts as models for target products, especially Cu-based carbon catalysts, deserves further exploration. Differently, the mass transfer of CO_2 also plays an important role in improving the current density. Some approaches can be utilized to overcome this problem in an aqueous solution: (1) performing this reaction in an organic solvent such as acetonitrile to promote the solubility of CO_2; (2) adjusting reaction systems, such as increasing reaction pressure to promote the solubility of CO_2; (3) designing new electrochemical cells, such as flow cell, overcoming the inherently low diffusion between CO_2 and the catalyst surface.

This review provides the guidance to explore promising strategies for the CO_2RR, so as to achieve high energy efficiency, industry-compatible current densities, and admirable conversion efficiency in the future. Inspiringly, carbon-based materials are expected to achieve the high performance towards the CO_2RR by combining the theory of computer science and quantum chemistry with experiments, which can significantly decrease the workload of researchers.

Declaration of competing interest

The authors declare that they have no known competing financial interests or personal relationships that could have appeared to influence the work reported in this paper.

Acknowledgments

This work was supported by the National Natural Science Foundation of China (No. 22071172), the Strategic Priority Research Program of the Chinese Academy of Sciences (No. XDB12030300), the Ministry of Science and Technology of China (Nos. 2017YFA0204503 and 2018YFA0703200).

References

[1] E. Dlugokencky, P. Tans, NOAA/ESRL, http://www.esrl.noaa.gov/gmd/ccgg/trends/, accessed: July 2021.
[2] F.P.G. De Arquer, C.T. Dinh, A. Ozden, et al., Science 367 (2020) 661–666.
[3] Y.S. Wu, Z. Jiang, X. Lu, Y.Y. Liang, H.L. Wang, Nature 575 (2019) 639–642.
[4] C.H. Yang, S.Y. Li, Z.C. Zhang, et al., Small 16 (2020) 2001847.
[5] N. Wang, R.K. Miao, G. Lee, et al., SmartMat 2 (2021) 12–16.
[6] H. Zhong, M. Ghorbani-Asl, K.H. Ly, et al., Nat. Commun. 11 (2020) 1–10.
[7] J.D. Yi, R. Xie, Z.L. Xie, et al., Angew. Chem. Int. Ed. 59 (2020) 23641–23648.
[8] O.S. Bushuyev, P. De Luna, C.T. Dinh, et al., Joule 2 (2018) 825–832.
[9] W.L. Zhu, R. Michalsky, O.N. Metin, et al., J. Am. Chem. Soc. 135 (2013) 16833–16836.
[10] D.F. Gao, T.F. Liu, G.X. Wang, X.H. Bao, ACS Energy Lett. 6 (2021) 713–727.
[11] Y.T. Zhu, X.Y. Cui, H.L. Liu, et al., Nano Res. 14 (2021) 4471–4486.
[12] L. Fan, C. Xia, F.Q. Yang, et al., Sci. Adv. 6 (2020) eaay3111.
[13] C.H. Yang, F. Nosheen, Z.C. Zhang, Rare Met. 40 (2021) 1412–1430.
[14] C. Xia, Y. Zhou, C. He, et al., Small Sci. 1 (2021) 2100010.
[15] L.M. Wang, W.L. Chen, D.D. Zhang, et al., Chem. Soc. Rev. 48 (2019) 5310–5349.
[16] J.T. Feaster, C. Shi, E.R. Cave, et al., ACS Catal. 7 (2017) 4822–4827.
[17] Y. Song, S. Wang, W. Chen, et al., ChemSusChem 13 (2020) 293–297.
[18] K. Zhao, X. Quan, ACS Catal. 11 (2021) 2076–2097.
[19] T. Chen, T.Y. Liu, X.Y. Shen, et al., Sci. China Mater. 64 (2021) 2997–3006.
[20] L. Fu, R. Wang, C. Zhao, et al., Chem. Eng. J. 414 (2021) 128857.
[21] T. Cheng, H. Xiao, W.A. Goddard, Proc. Natl. Acad. Sci. 114 (2017) 1795–1800.
[22] Y.J. Zhao, L.L. Zheng, D. Jiang, et al., Small 17 (2021) 2006590.
[23] I. Ledezma-Yanez, E.P. Gallent, M.T. Koper, F. Calle-Vallejo, Catal. Today 262 (2016) 90–94.
[24] N. Han, P. Ding, L. He, Y. Li, Y. Li, Adv. Energy Mater. 10 (2020) 2070046.
[25] H. Xu, D. Cheng, D. Cao, X.C. Zeng, Nat. Catal. 1 (2018) 339–348.
[26] H.B. Yang, S.F. Hung, S. Liu, et al., Nat. Energy 3 (2018) 140–147.
[27] H.W. Hu, J.H. Xin, H. Hu, X.W. Wang, Y. Kong, Appl. Catal. A: Gen. 492 (2015) 1–9.
[28] D.S. Su, S. Perathoner, G. Centi, Chem. Rev. 113 (2013) 5782–5816.
[29] K. Jiang, S. Siahrostami, A.J. Akey, et al., Chem 3 (2017) 950–960.
[30] B. Kumar, M. Asadi, D. Pisasale, et al., Nat. Commun. 4 (2013) 2819.
[31] J. Wu, R.M. Yadav, M. Liu, et al., ACS Nano 9 (2015) 5364–5371.
[32] H. Wang, J. Jia, P.F. Song, et al., Angew. Chem. Int. Ed. 56 (2017) 7847–7852.
[33] J.Y. Xu, Y.H. Kan, R. Huang, et al., ChemSusChem 9 (2016) 1085–1089.
[34] H.X. Wang, Y.B. Chen, X.L. Hou, C.Y. Ma, T.W. Tan, Green Chem. 18 (2016) 3250–3256.
[35] J.J. Wu, M.J. Liu, P.P. Sharma, et al., Nano Lett. 16 (2016) 466–470.
[36] H.P. Yang, Y. Wu, Q. Lin, et al., Angew. Chem. Int. Ed. 57 (2018) 15476–15480.
[37] B.X. Zhang, J.L. Zhang, F.Y. Zhang, et al., Adv. Funct. Mater. 30 (2020) 1906194.
[38] J.F. Xie, X.T. Zhao, M.X. Wu, et al., Angew. Chem. Int. Ed. 57 (2018) 9640–9644.
[39] M. Kuang, A.X. Guan, Z.X. Gu, et al., Nano Res. 12 (2019) 2324–2329.
[40] B.B. Pan, X.R. Zhu, Y.L. Wu, et al., Adv. Sci. 7 (2020) 2001002.
[41] J.J. Wu, S.C. Ma, J. Sun, et al., Nat. Commun. 7 (2016) 13869.
[42] P.P. Sharma, J.J. Wu, R.M. Yadav, et al., Angew. Chem. Int. Ed. 54 (2015) 13701–13705.
[43] X.L. Zou, M.J. Liu, J.J. Wu, et al., ACS Catal. 7 (2017) 6245–6250.
[44] L.M. Azofra, D.R. MacFarlane, C.H. Sun, Phys. Chem. Chem. Phys. 18 (2016) 18507–18514.
[45] X.Y. Lu, T.H. Tan, Y.H. Ng, R. Amal, Chem. Eur. J. 22 (2016) 11991–11996.
[46] X. Zhi, Y. Jiao, Y. Zheng, S.Z. Qiao, Small 15 (2019) 1804224.
[47] Y.M. Liu, S. Chen, X. Quan, H.T. Yu, J. Am. Chem. Soc. 137 (2015) 11631–11636.
[48] Y.M. Liu, Y.J. Zhang, K. Cheng, et al., Angew. Chem. 129 (2017) 15813–15817.
[49] O.A. Baturina, Q. Lu, M.A. Padilla, et al., ACS Catal. 4 (2014) 3682–3695.
[50] R. Daiyan, W.H. Saputera, H. Masood, et al., Adv. Energy Mater. 10 (2020) 1902106.
[51] Y.Q. Su, H.T. Xu, J.J. Wang, et al., Nano Res. 12 (2019) 625–630.
[52] M. Zhu, L. Zhang, S. Liu, et al., Chin. Chem. Lett. 31 (2020) 1961–1965.
[53] C.H. Yang, Z.Q. Gao, W. Dingjia, et al., Sci. China Mater. 65 (2022) 155–162.
[54] M. Gangeri, S. Perathoner, S. Caudo, et al., Catal. Today 143 (2009) 57–63.
[55] X. Wang, Z.Y. Wang, F.P. García de Arquer, et al., Nat. Energy 5 (2020) 478–486.
[56] H. Zhong, F. Meng, Q. Zhang, K. Liu, X. Zhang, Nano Res. 12 (2019) 2318–2323.
[57] J.J. Sun, W.Z. Zheng, S.L. Lyu, et al., Chin. Chem. Lett. 31 (2020) 1415–1421.
[58] J. Du, S.P. Li, S.L. Liu, et al., Chem. Sci. 11 (2020) 5098–5104.
[59] Y. Jiao, Y. Zheng, P. Chen, M. Jaroniec, S.Z. Qiao, J. Am. Chem. Soc. 139 (2017) 18093–18100.
[60] L. Zhang, F.X. Mao, L.R. Zheng, et al., ACS Catal. 8 (2018) 11035–11041.
[61] Q. Xu, J. Zhang, D. Wang, Y. Li, Chin. Chem. Lett. 32 (2021) 3771–3781.
[62] N. Zhang, X. Zhang, L. Tao, et al., Angew. Chem. Int. Ed. 60 (2021) 6170–6176.
[63] A.Q. Wang, J. Li, T. Zhang, Nat. Rev. Chem. 2 (2018) 65–81.
[64] Y. Shang, X. Xu, B. Gao, S. Wang, X. Duan, Chem. Soc. Rev. 50 (2021) 5281–5322.
[65] L. Gong, H. Yang, H. Wang, et al., Nano Res. 14 (2021) 4528–4533. https://link.springer.com/article/10.1007/s12274-021-3366-3.
[66] X.F. Yang, A.Q. Wang, B.T. Qiao, et al., Acc. Chem. Res. 46 (2013) 1740–1748.
[67] Y.J. Chen, S.F. Ji, C. Chen, et al., Joule 2 (2018) 1242–1264.
[68] B.T. Qiao, A.Q. Wang, X.F. Yang, et al., Nat. Chem. 3 (2011) 634–641.
[69] S. Meshitsuka, M. Ichikawa, K. Tamaru, J. Chem. Soc. Chem. Commun. (1974) 158–159.
[70] X. Yan, D.L. Liu, H.H. Cao, et al., Small Methods 3 (2019) 1800501.
[71] F.P. Pan, H.G. Zhang, K.X. Liu, et al., ACS Catal. 8 (2018) 3116–3122.
[72] D.W. Stephan, Acc. Chem. Res. 48 (2015) 306–316.
[73] Y.D. Li, Sci. China Mater. 59 (2016) 1.
[74] J. Yang, W. Li, D. Wang, Y. Li, Small Struct. 2 (2021) 2000051.
[75] Z.X. Wang, J.X. Zhao, Q.H. Cai, Phys. Chem. Chem. Phys. 19 (2017) 23113–23121.
[76] A. Bagger, W. Ju, A.S. Varela, P. Strasser, J. Rossmeisl, Catal. Today 288 (2017) 74–78.
[77] V. Tripkovic, M. Vanin, M. Karamad, et al., J. Phys. Chem. C 117 (2013) 9187–9195.
[78] F.P. Pan, W. Deng, C. Justiniano, Y. Li, Appl. Catal. B: Environ. 226 (2018) 463–472.
[79] H.L. Liu, Y.T. Zhu, J.M. Ma, Z.C. Zhang, W.P. Hu, Adv. Funct. Mater. 30 (2020) 1910534.
[80] W. Yang, Y. Zhu, J. Li, et al., Chin. Chem. Lett. 32 (2021) 286–290.
[81] G. Wan, G.H. Zhang, X.M. Lin, Adv. Mater. 32 (2020) 1905548.
[82] A.S. Varela, N. Ranjbar Sahraie, J. Steinberg, et al., Angew. Chem. Int. Ed. 54 (2015) 10758–10762.
[83] X.G. Li, W.T. Bi, M.L. Chen, et al., J. Am. Chem. Soc. 139 (2017) 14889–14892.
[84] J. Gu, C.S. Hsu, L.C. Bai, H.M. Chen, X.L. Hu, Science 364 (2019) 1091–1094.
[85] H. Shang, T. Wang, J. Pei, et al., Angew. Chem. Int. Ed. 59 (2020) 22465–22469.
[86] J. Yang, Z.Y. Qiu, C.M. Zhao, et al., Angew. Chem. Int. Ed. 57 (2018) 14095–14100.

[87] Y. Pan, R. Lin, Y. Chen, S. Liu, et al., J. Am. Chem. Soc. 140 (2018) 4218–4221.
[88] W. Ju, A. Bagger, G.P. Hao, et al., Nat. Commun. 8 (2017) 944.
[89] K. Xu, S. Zheng, Y. Li, et al., Chin. Chem. Lett. 33 (2022) 424–427.
[90] C. Huang, J.H. Liu, H.H. Huang, X.F. Xu, Z.F. Ke, Chin. Chem. Lett. 33 (2022) 262–265.
[91] H. Furukawa, K.E. Cordova, M. O'Keeffe, O.M. Yaghi, Science 341 (2013) 1230444.
[92] N. Stock, S. Biswas, Chem. Rev. 112 (2012) 933–969.
[93] M.Y. Gao, B.Q. Song, D. Sensharma, M.J. Zaworotko, SmartMat 2 (2021) 38–55.
[94] H.B. Meng, Y. Han, C.H. Zhou, et al., Small Methods 4 (2020) 2000396.
[95] S.R. Ahrenholtz, C.C. Epley, A.J. Morris, J. Am. Chem. Soc. 136 (2014) 2464–2472.
[96] I. Hod, M.D. Sampson, P. Deria, et al., ACS Catal. 5 (2015) 6302–6309.
[97] J. Albo, D. Vallejo, G. Beobide, et al., ChemSusChem 10 (2017) 1100–1109.
[98] B.X. Dong, S.L. Qian, F.Y. Bu, et al., ACS Appl. Energy Mater. 1 (2018) 4662–4669.
[99] L. Ye, J.X. Liu, Y. Gao, et al., J. Mater. Chem. A 4 (2016) 15320–15326.
[100] K. Zhao, Y.M. Liu, X. Quan, S. Chen, H.T. Yu, ACS Appl. Mater. Interfaces 9 (2017) 5302–5311.
[101] M. Perfecto-Irigaray, J. Albo, G. Beobide, et al., RSC Adv. 8 (2018) 21092–21099.
[102] C.M. Zhao, Dai X.Y, T. Yao, et al., J. Am. Chem. Soc. 139 (2017) 8078–8081.
[103] Y.L. Qiu, H.X. Zhong, T.T. Zhang, et al., ACS Appl. Mater. Interfaces 10 (2018) 2480–2489.
[104] Y. Cheng, S.Y. Zhao, B. Johannessen, et al., Adv. Mater. 30 (2018) 1706287.
[105] Y. Zhang, L. Jiao, W.J. Yang, C.F. Xie, H.L. Jiang, Angew. Chem. Int. Ed. 60 (2021) 7607–7611.
[106] N. Kornienko, Y.B. Zhao, C.S. Kley, et al., J. Am. Chem. Soc. 137 (2015) 14129–14135.
[107] Y.T. Guntern, J.R. Pankhurst, J. Vávra, et al., Angew. Chem. Int. Ed. 58 (2019) 12632–12639.
[108] E.H. Zhang, T. Wang, K. Yu, et al., J. Am. Chem. Soc. 141 (2019) 16569–16573.
[109] L.S. Xie, G. Skorupskii, M. Dincă, Chem. Rev. 120 (2020) 8536–8580.
[110] Z.Q. Gao, C.Y. Wang, J.J. Li, et al., Acta Phys. Chim. Sin. 37 (2021) 2010025-2010020.
[111] L. Majidi, A. Ahmadiparidari, N. Shan, et al., Adv. Mater. 33 (2021) 2004393.
[112] L. Dai, Q. Qin, P. Wang, et al., Sci. Adv. 3 (2017) e1701069.
[113] W. Fang, L. Huang, S. Zaman, et al., Chem. Res. Chin. Univ. 36 (2020) 611–621.
[114] D.H. Nam, O. Shekhah, G. Lee, et al., J. Am. Chem. Soc. 142 (2020) 21513–21521.
[115] N. Wang, K.L. Yao, A. Vomiero, Y. Wang, H. Liang, SmartMat 2 (2021) 423–425.
[116] F.W. Li, Y.C. Li, Z.Y. Wang, et al., Nat. Catal. 3 (2020) 75–82.
[117] Y.H. Wang, W.J. Jiang, W. Yao, et al., Rare Met. 40 (2021) 2327–2353.
[118] C.S. Cao, D.D. Ma, J.F. Gu, et al., Angew. Chem. Int. Ed. 59 (2020) 15014–15020.
[119] P. Lamagni, M. Miola, J. Catalano, et al., Adv. Funct. Mater. 30 (2020) 1910408.
[120] X.R. Zhang, Y.X. Zhang, Q.Q. Li, et al., J. Mater. Chem. A 8 (2020) 9776–9787.
[121] Z. Yang, H. Wang, X. Fei, et al., Appl. Catal. B: Environ. (2021) 120571.
[122] X.H. Zhao, Q.S. Chen, D.H. Zhuo, et al., Electrochim. Acta 367 (2021) 137478.
[123] S.G. Han, D.D. Ma, Q.L. Zhu, Small Methods 5 (2021) 2100102.
[124] D.Z. Yao, C. Tang, A. Vasileff, et al., Angew. Chem. Int. Ed. 60 (2021) 18178–18184.